Distortion-Free Zeeman Torque Sampling for Detecting Terahertz Magnetic Field Pulse

Chun-yan Geng(耿春艳)[1,2], Yi-chen Su(苏一辰)[3], De-yin Kong(孔德胤)[1,2,4], Fei Dai(戴飞)[2], Cheng-song(宋成)[3], and Xiao-jun Wu(吴晓君)[1,2,4,5*]

[1]*Hangzhou International Innovation Institute, Beihang University, Hangzhou 311115, China*
[2]*School of Electronic and Information Engineering, Beihang University, Beijing 100191, China*
[3]*Key Laboratory of Advanced Materials (MOE), School of Materials Science and Engineering, Tsinghua University, Beijing 100084, China*
[4]*Zhangjiang Laboratory, Shanghai 201210, China*
[5]*Wuhan National Laboratory for Optoelectronics, Huazhong University of Science and Technology, Wuhan 430074, China*

(Received 1 August 2025; accepted manuscript online 17 September 2025)

Strong-field terahertz (THz) radiation holds significant potential in non-equilibrium state manipulation, electron acceleration, and biomedical effects. However, distortion-free detection of strong-field THz waveforms remains an essential challenge in THz science and technology. To address this issue, we propose a ferromagnetic detection scheme based on Zeeman torque sampling, achieving distortion-free strong-field THz waveform detection in Py films. Thickness-dependent characterization (3–21 nm) identifies peak detection performance at 21 nm within the investigated range. Furthermore, by structurally engineering the Py ferromagnetic layer, we demonstrate strong-field THz detection in symmetric Ta(3 nm)/Py(9 nm)/Ta(3 nm) heterostructure while simultaneously resolving Zeeman torque responses and collective spin-wave dynamics in asymmetric W(4 nm)/Py(9 nm)/Pt(2 nm) heterostructure. We calculated spin wave excitations and spin orbit torque distributions in asymmetric heterostructures, along with spin wave excitations in symmetric modes. This approach overcomes the sensitivity limitations of conventional techniques in strong-field conditions.

DOI: 10.1088/0256-307X/42/11/110802 CSTR: 32039.14.0256-307X.42.11.110802

Occupying the spectral region between microwaves and infrared light, terahertz (THz) radiation exhibits unique electromagnetic properties that demonstrate significant application potential across diverse fields including THz communication,[1–5] imaging perception,[6–10] and quantum state manipulation.[11–17] Crucially, advances in high-power femtosecond laser technology have enabled laser-driven THz sources to achieve pulse energies on the millijoule (mJ) scale,[18–21] with peak electric fields advancing from kV/cm to MV/cm regimes.[22,23] This progression has shifted THz-matter interactions from weak-field linear responses to strong-field nonlinear control. The interaction between strong-field THz radiation and matter can realize the non-equilibrium state of matter,[24–28] the coherent control of electron spin[29–31] and the nonlinearity of phonons.[32,33] These capabilities are essential for advancing fundamental research and technological innovation. However, it is a major challenge to accurately detect the collective excitation of strong-field THz and magnetic order under strong-field conditions, which is crucial for understanding the interaction between THz magnetic fields and matter and developing high-performance THz devices.

Current strong-field THz detection methodologies primarily encompass detecting THz pulses via thermal effects, field-sensitive detection using Schottky diodes with nonlinear current-voltage characteristics. Although these techniques partially satisfy detection requirements, they exhibit significant limitations in strong-field environments, impeding precise capture of temporal pulse distributions and subtle variations. While electro-optic sampling (EOS) offers enhanced sensitivity for THz electric field component detection,[34,35] this technique is constrained by linear electro-optic saturation, particularly when excessive polarization rotation of probe induces waveform distortion, thereby compromising accurate characterization of strong-field THz pulses. Recently, a spintronic detector comprising FM|HM heterostructures has been proposed,[36] enabling direct spintronic sampling via THz electric field driven spin accumulation at FM|HM interfaces through the spin Rashba–Edelstein effect, which generates detectable birefringence signals. This method represents a significant advancement in THz field detection but requires further decoupling of the acquired birefringence signals. Consequently, developing a simple, direct-sampling methodology for THz waveform detection remains an imperative pursuit.

In this paper, we present a magnetic field component

*Corresponding author. Email: xiaojunwu@buaa.edu.cn
© 2025 Chinese Physical Society and IOP Publishing Ltd. All rights, including for text and data mining, AI training, and similar technologies, are reserved.

detection technique based on Zeeman torque sampling, utilizing Py ferromagnetic films as detectors for strong-field THz waves. Upon interaction with the strong-field THz radiation, the induced Zeeman torque drives dynamic reconstruction of the magnetization state within the Py film. These magnetization dynamics are probed indirectly via the Faraday rotation effect, enabling precise measurement of the THz magnetic field components. Zeeman torque, which is associated with the magnetic field component of THz pulses, drives the detected signal. The detection capability of ferromagnetic films exhibits thickness-dependent enhancement within the 3–21 nm range, peaking at 21 nm for Py. Moreover, we observed a more significant phenomenon in the heterostructures: the symmetric Ta(3 nm)/Py(9 nm)/Ta(3 nm) configuration achieved distortion-free detection of strong-field THz waveforms, while the asymmetric W(4 nm)/Py(9 nm)/Pt(2 nm) heterostructure exhibited a Zeeman torque induced main peak with accompanying oscillatory spin waves in the tail. Through systematic analysis, we elucidated the excitation mechanism of spin waves, the spin orbit torque (SOT) distribution, and identified the origin of non-zero detection signals in symmetric modes. Compared with the previous work,[36] a single-layer ferromagnetic film enables the detection of THz magnetic fields, while a triple-layer ferromagnetic heterostructure facilitates dual detection of both the primary Zeeman torque peak and spin wave signals. This method establishes a new way for strong-field THz detection technology.

Advancing high-power THz sources requires complementary detection capabilities. Currently, EOS serves as the primary technique for THz waveforms detection, leveraging the linear electro-optic effect in ZnTe crystals.[34,35] EOS achieves excellent THz waveform detection in weak-field, but suffers from waveform distortion caused by oversaturation in strong-field [see Section S1 of the Supplementary Materials (SM)]. To overcome this limitation, we propose Zeeman torque sampling—a technique detecting THz magnetic field components via interaction with ferromagnetic films.

We employed a strong-field THz pump-optical Faraday detection system driven by a Ti: sapphire laser (800 nm center wavelength, 35 fs pulse duration, 1 kHz repetition rate), as illustrated in Fig. 1(a). The laser beam is initially split by a beamsplitter into a pump beam (90% intensity) and a probe beam (10% intensity), the pump is incident

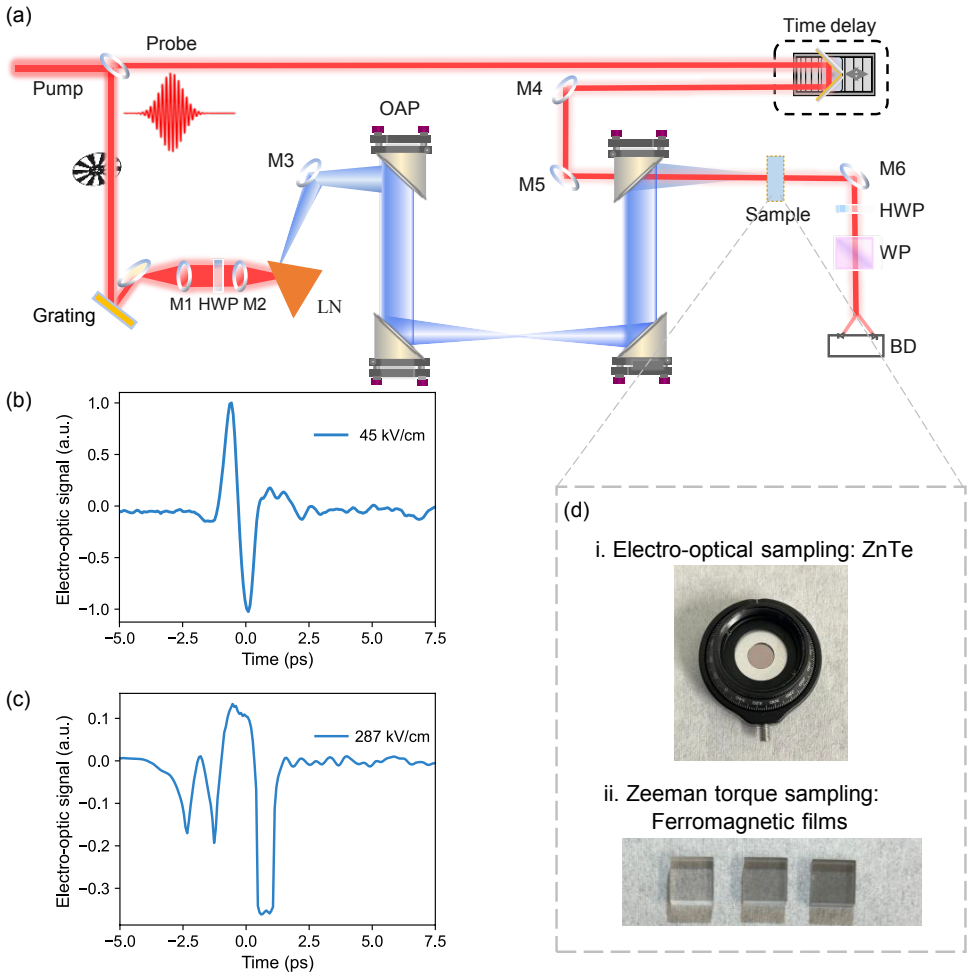

Fig. 1. THz waveform measurement. (a) Experimental setup. (b) Weak-field and (c) Strong-field THz waveforms acquired via EOS, the conventional electro-optic detection leads to major distortions, as clearly seen in panel (c). (d) Comparative methodologies: EOS (implemented via birefringence in ZnTe crystals), Zeeman torque sampling (THz magnetic component interaction with monolayer ferromagnetic films). Panel i: ZnTe crystal. Panel ii: ferromagnetic films (from left to right: 3 nm, 5 nm, and 9 nm).

on the grating at a specific angle, then passes through a 4f system to reach the lithium niobate crystal. Here, optical rectification generates THz radiation, which is collected by four off-axis parabolic (OAP) mirrors. At the detection plane, the collinear probe and THz pulses are normally incident on the selected detector (electro-optical crystal or ferromagnetic film). Subsequently, the modulated probe is detected via a half-wave plate and Wollaston prism for polarization-resolved balanced detection. When employing a nonlinear electro-optic crystal as a detector, we utilize its intrinsic birefringence effect for real-time THz detection. Figures 1(b) and 1(c) present time-domain waveforms obtained by the ZnTe crystal in weak-field and strong field. Under a field strength of 45 kV/cm, the EOS signal can be easily detected using a 0.5 mm-thick ZnTe crystal. However, under strong fields, conventional EOS may lead to severe waveform distortion, as shown in Fig. 1(c). Figure 1(d) comparatively illustrates the two detector schemes: Panel (i) shows a photographic image of the 0.5 mm-thick ZnTe crystal; while Panel (ii) displays ferromagnetic films with different thicknesses (3 nm, 5 nm, and 9 nm, from left to right).

Using the setup in Fig. 2(a) with picosecond resolution, we tracked ultrafast magnetization dynamics via collinear pump-probe geometry: strong-field THz pulses excited the Py sample while 800 nm femtosecond laser detected Faraday rotation signals perpendicular to the film plane. In our experiments, an external magnetic field is required. For soft magnetic materials such as Py films, an external field is necessary to align the magnetization in a consistent orientation. The THz-driven Zeeman torque induces out-of-plane magnetization reorientation in Py films. Through differential analysis of raw signals, we extracted THz-induced dynamics, which obey the Landau–Lifshitz–Gilbert (LLG) equation as

$$\frac{\mathrm{d}\boldsymbol{m}_{\mathrm{py}}}{\mathrm{d}t} = -\gamma \boldsymbol{m}_{\mathrm{py}} \times \boldsymbol{B}_{\mathrm{eff}} + \alpha \boldsymbol{m}_{\mathrm{py}} \times \frac{\mathrm{d}\boldsymbol{m}_{\mathrm{py}}}{\mathrm{d}t}, \tag{1}$$

where $\boldsymbol{m}_{\mathrm{py}}$, $\boldsymbol{B}_{\mathrm{eff}}$, γ, and α refer to the unit magnetization, the effective magnetic field, the electron gyromagnetic ratio, and the Gilbert damping factor. Decomposing the unit magnetization vector $\boldsymbol{m}_{\mathrm{py}} = \boldsymbol{m}_0 + \boldsymbol{m}$, where $\boldsymbol{m}_0$ is the equilibrium component satisfying $\frac{\mathrm{d}\boldsymbol{m}_0}{\mathrm{d}t} = 0$ and $\boldsymbol{m}$ is the change of $\boldsymbol{m}_{\mathrm{py}}$, $|\boldsymbol{m}| \ll 1$, and $\boldsymbol{B}_{\mathrm{eff}} = \boldsymbol{B}_0 + \boldsymbol{B}_{\mathrm{THz}}$, $\boldsymbol{B}_0$ is the static field, which includes the external magnetic field, the demagnetizing field and the anisotropy field, $\boldsymbol{B}_{\mathrm{THz}}$ is the THz magnetic field. As $\boldsymbol{B}_{\mathrm{eff}}$ is a function of $\boldsymbol{m}_{\mathrm{py}}$, linearization yields

$$\frac{\mathrm{d}\boldsymbol{m}}{\mathrm{d}t} = -\gamma \boldsymbol{m}_0 \times \boldsymbol{B}_{\mathbf{THz}} + \boldsymbol{W} \cdot \boldsymbol{m} + D\frac{\mathrm{d}\boldsymbol{m}}{\mathrm{d}t}. \tag{2}$$

The matrix $\boldsymbol{W}$ governs ferromagnetic resonance in Py ($\omega_0 \sim$ GHz), while $D \propto \alpha$ represents damping matrix. Crucially, the large THz-ferromagnetic frequency mismatch $|\boldsymbol{W} \cdot \boldsymbol{m}| \ll |-\gamma \boldsymbol{m}_0 \times \boldsymbol{B}_{\mathrm{THz}}|$ and weak damping ($\alpha \ll 1$) enable significant simplification. Neglecting D and the resonant term reduces the dynamics to

$$\frac{\mathrm{d}\boldsymbol{m}}{\mathrm{d}t} = -\gamma \boldsymbol{m}_0 \times \boldsymbol{B}_{\mathrm{THz}}. \tag{3}$$

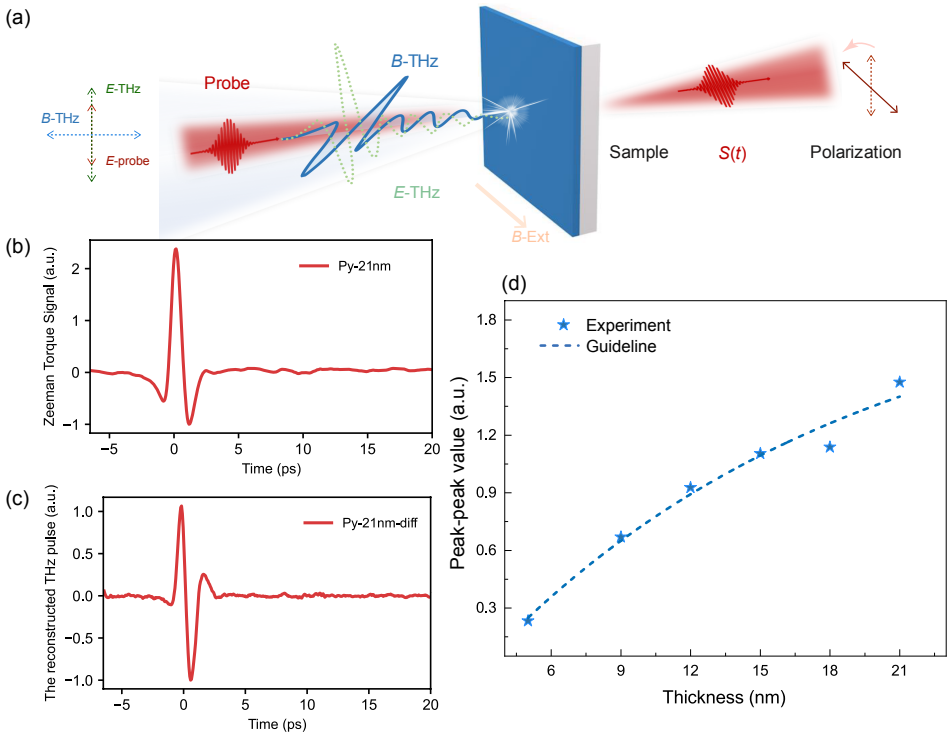

Fig. 2. Zeeman torque sampling schematic diagram. (a) Schematic of the THz pump-optical Faraday technique. The THz magnetic field component (blue curve) and the 800 nm probe (red curve) with collinear propagation and perpendicular incidence on the sample. The 800 nm probe pulses are in reality much shorter than the THz pulses. (b) The magnetization kinetics curve of a single-layer ferromagnetic film Py-21nm. (c) THz waveform after time derivative from raw data. (d) Relation between the peak-to-peak signal and the thickness of a single-layer Py ferromagnetic film. The dashed line serves as a guideline.

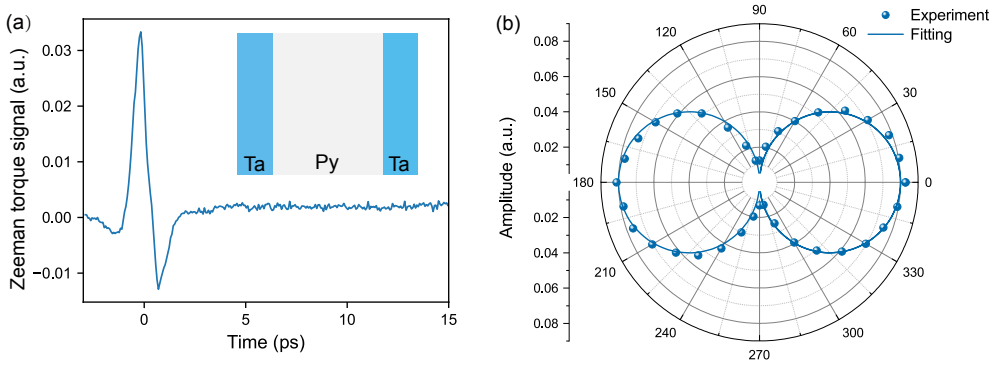

Fig. 3. Symmetric heterojunction dynamics results. (a) Ta(3 nm)/Py(9 nm)/Ta(3 nm) trilayer symmetric heterostructure detection. (b) Azimuthal dependence: Peak-to-peak amplitudes of magnetization dynamics extracted at angles through simultaneous rotation of the external magnetic field and sample orientation.

Overall, when the driving THz frequency substantially exceeds the system intrinsic ferromagnetic resonance frequency in Py, magnetic moments operate in a non-resonant response regime. Here, the instantaneous magnetization dynamics are directly torque-driven, satisfying Eq. (3). It is obvious that the time derivatives of $\boldsymbol{m}$ are proportional to $\boldsymbol{B}_{\mathrm{THz}}$. Consequently, applying this derivative processing to the Fig. 2(b) data yields the reconstructed THz signal shown in Fig. 2(c). This approach enables faithful extraction of strong-field THz time-domain waveforms, critically addressing the saturation-induced distortion inherent in nonlinear electro-optic crystals under strong-field conditions.

To investigate the thickness-related effects in ferromagnetic detectors, we systematically varied Py film thicknesses from 3 nm to 21 nm. Subsequently, we measured Zeeman torque signals across varying film thicknesses and extracted corresponding peak-to-peak amplitudes. As illustrated in Fig. 2(d), the experimental amplitude data show progressive enhancement with increasing Py thickness, and the dashed line is a guide to the eye. The largest signal was observed at a Py thickness of 21 nm, which was the maximum value fabricated in this study. However, the potential applicability of thicker films cannot be ruled out. The aberrant THz signal observed in the 18 nm Py film is likely attributable to sample-specific variations. Furthermore, we directly compare EOS and Zeeman torque sampling under identical weak and strong THz field strengths (see Section S2 of the SM). This distortion-free THz waveform detection technology provides a feasible path for the application development of strong-field THz.

To further explore the THz detection capabilities of ferromagnetic films in different structures and their underlying ultrafast dynamics, we have reconfigured the single-layer system into a symmetric Ta(3 nm)/Py(9 nm)/Ta(3 nm) trilayer heterostructure. In this architecture, Ta layers with strong spin orbit coupling symmetrically flank the Py interlayer, permitting THz transient penetration while the Py layer retains in-plane magnetization at equilibrium. Upon THz excitation, the electric field component drives charge currents in Ta layers that convert to spin currents via spin Hall effect and inject into Py. While spin accumulation occurs at the interfaces, the symmetric Ta overlayer configuration cancels net spin polarization. Concurrently, the transient THz magnetic field drives the magnetization vector via Zeeman interaction, generating an out-of-plane component that initiates nonequilibrium precession of magnetic moments within the Py layer. This magnetization evolution confirms detectable dynamics in symmetric heterostructures via Faraday rotation modulation of the 800 nm probe polarization, enabling picosecond-resolution THz magnetic field detection. Figure 3(a) demonstrates consistent strong-field THz detection capability via Zeeman torque sampling in symmetric heterostructures.

To explore the THz polarization dependence in symmetric heterojunction, we modulate the THz polarization equivalently in 10° increments by synchronous rotation of the external magnetic field and sample azimuth in a range of 0°–360°. The azimuth is defined as the angle between the THz electric field and the external magnetic field (Py magnetization). The 0° means the THz electric field is parallel to the magnetization of Py, and the 180° means the reversal of Py magnetization. Figure 3(b) shows the peak-to-peak amplitude of the magnetization dynamics curves extracted from the Ta(3 nm)/Py(9 nm)/Ta(3 nm) sample at different azimuths, revealing that the Zeeman torque signal is symmetrical with a period of 90°. This phenomenon primarily arises from the fact that when the azimuth angle changes, the effective field and the crystal direction of the magnetization axis of the heterojunction sample form different angles. This variation, in turn, regulates the suppression of the magnetic moment's precession amplitude by magnetocrystalline anisotropy. The Zeeman torque signal peaks at 0° and 180° azimuthal angles, while exhibiting significant attenuation at 90° and 270° directions. This attenuation may arise from the non-ideal polarization of THz. These measurements conclusively demonstrate ultrafast magnetization dynamics in Ta(3 nm)/Py(9 nm)/Ta(3 nm) heterostructures driven by THz magnetic field components via Zeeman interactions at picosecond timescales.

To further elucidate the structural determinants of strong-field THz coupling in metallic heterostructures, the

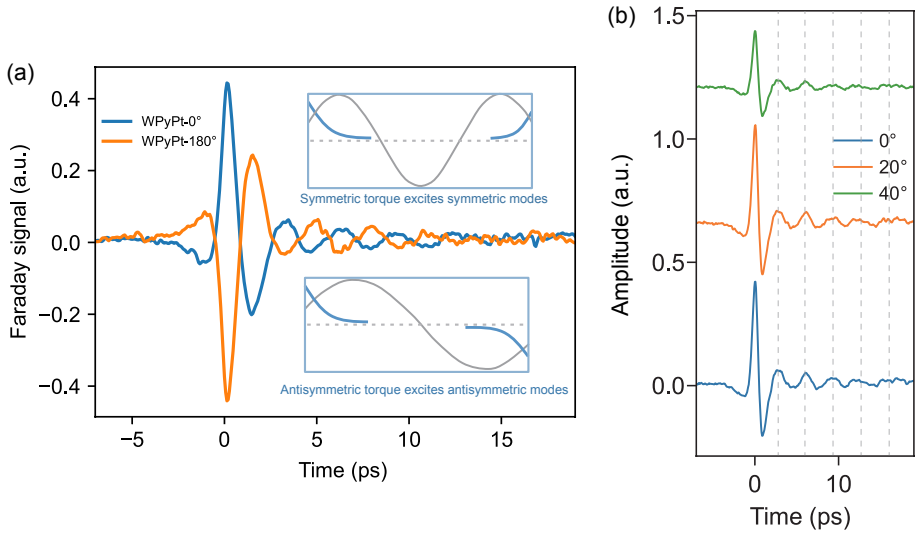

Fig. 4. Asymmetric heterojunction dynamics results. (a) Spin waves observed in the W(4 nm)/Py(9 nm)/Pt(2 nm) trilayer structure. The illustration shows symmetric torque excites symmetric modes and antisymmetric torque excites antisymmetric modes, where the blue line represents SOT distribution and the gray line represents Potential magnon modes. (b) Signals under different THz field strengths obtained by attenuating THz intensity with a pair of polarizers.

symmetric Ta(3 nm)/Py(9 nm)/Ta(3 nm) structure was replaced by an asymmetric W(4 nm)/Py(9 nm)/Pt(2 nm) heterostructure with opposite spin Hall angles, enabling investigation of structural effects on strong-field THz coupling. Figure 4(a) presents the Faraday signals of the asymmetric heterostructure, revealing a response distinct from symmetric configurations, the Faraday signal of the asymmetric sample consists of two parts, the first part is the main peak caused by the Zeeman torque, while the second arises from spin wave excitation. The presence of a spin wave signal does not directly correspond to the actual THz waveform (see Section S3 of the SM). For W(4 nm)/Py(9 nm)/Pt(2 nm) samples, the SOT tends to be a symmetric distribution. Considering the LLG equation, we have

$$\begin{aligned}\frac{\mathrm{d}\boldsymbol{m}_{\mathrm{py}}}{\mathrm{d}t} =& -\gamma\boldsymbol{m}_{\mathrm{py}}\times\boldsymbol{B}-2\gamma A\boldsymbol{m}_{\mathrm{py}}\times\nabla^2\boldsymbol{m}_{\mathrm{py}}\\ &+\alpha\boldsymbol{m}_{\mathrm{py}}\times\frac{\mathrm{d}\boldsymbol{m}_{\mathrm{py}}}{\mathrm{d}t}+\boldsymbol{\tau},\end{aligned}\tag{4}$$

where $\boldsymbol{m}_{\mathrm{py}}$, $\boldsymbol{B}$, A and $\boldsymbol{\tau}$ are the direction of magnetization, the external magnetic field, the exchange stiffness, and the SOT, respectively. In W(4 nm)/Py(9 nm)/Pt(2 nm) samples, $\boldsymbol{\tau}$ has an approximate symmetric distribution shown in the upper part of Fig. 4(a), and can be described as $\boldsymbol{\tau}=\boldsymbol{P}\mathrm{e}^{x/\lambda}+\boldsymbol{Q}\mathrm{e}^{-x/\lambda}$, where $\boldsymbol{P}$ and $\boldsymbol{Q}$ are the SOT strength at Pt/Py and Py/W interfaces with the same direction. λ refers to the spin diffusion length in Py, typically ∼4 nm. We define $\boldsymbol{m}_{\mathrm{py}}=\boldsymbol{m}_0+\boldsymbol{m}$, where the definitions of $\boldsymbol{m}_0$ and $\boldsymbol{m}$ are consistent with Eq. (2). After ignoring the higher-order terms, The LLG equation can be written as

$$\frac{\mathrm{d}\boldsymbol{m}}{\mathrm{d}t}=-\gamma\boldsymbol{m}\times\boldsymbol{B}-2\gamma A\boldsymbol{m}_0\times\nabla^2\boldsymbol{m}+\alpha\boldsymbol{m}_0\times\frac{\mathrm{d}\boldsymbol{m}}{\mathrm{d}t}+\boldsymbol{\tau}.\tag{5}$$

The excitation of spin waves needs both frequency matching and wave vector matching. Considering a certain frequency ω, included in the wave packet of THz pulses, we do the spatial Fourier transform of both $\boldsymbol{m}$ and $\boldsymbol{\tau}$. We define z direction as the $\boldsymbol{m}_0$ direction, and x direction as the film normal direction. We have $\boldsymbol{m}=\sum\boldsymbol{m}_k\mathrm{e}^{\mathrm{i}kx}\mathrm{e}^{-\mathrm{i}\omega t}$ and $\boldsymbol{\tau}=\sum\boldsymbol{\tau}_k\mathrm{e}^{\mathrm{i}kx}\mathrm{e}^{-\mathrm{i}\omega t}$. Here, $\boldsymbol{m}_k$ and $\boldsymbol{\tau}_k$ are the Fourier components of $\boldsymbol{m}$ and $\boldsymbol{\tau}$. For arbitrary k, equation (5) can be rewritten as

$$\begin{aligned}-\mathrm{i}\omega\boldsymbol{m}_k=&-\gamma\boldsymbol{m}_k\times\boldsymbol{B}+2\gamma Ak^2\boldsymbol{m}_0\times\boldsymbol{m}_k\\ &-\mathrm{i}\omega\alpha\boldsymbol{m}_0\times\boldsymbol{m}_k+\boldsymbol{\tau}_k.\end{aligned}\tag{6}$$

This equation is solvable, indicating that $\boldsymbol{\tau}_k$ can only excite $\boldsymbol{m}_k$ and can be calculated as

$$\boldsymbol{\tau}_k=\int_{-\frac{d}{2}}^{\frac{d}{2}}(\boldsymbol{P}\mathrm{e}^{x/\lambda}+\boldsymbol{Q}\mathrm{e}^{-x/\lambda})\mathrm{e}^{-\mathrm{i}kx}\mathrm{d}x,\tag{7}$$

where d is the thickness of Py layer. Therefore, we have

$$\begin{aligned}\boldsymbol{\tau}_k=&\frac{\lambda\boldsymbol{P}}{d(1-\mathrm{i}k\lambda)}[\mathrm{e}^{\frac{d}{2\lambda}(1-\mathrm{i}k\lambda)}-\mathrm{e}^{-\frac{d}{2\lambda}(1-\mathrm{i}k\lambda)}]\\ &-\frac{\lambda\boldsymbol{Q}}{d(1+\mathrm{i}k\lambda)}[\mathrm{e}^{-\frac{d}{2\lambda}(1+\mathrm{i}k\lambda)}-\mathrm{e}^{\frac{d}{2\lambda}(1+\mathrm{i}k\lambda)}],\end{aligned}\tag{8}$$

$$\begin{aligned}\boldsymbol{\tau}_{-k}=&\frac{\lambda\boldsymbol{P}}{d(1+\mathrm{i}k\lambda)}[\mathrm{e}^{\frac{d}{2\lambda}(1+\mathrm{i}k\lambda)}-\mathrm{e}^{-\frac{d}{2\lambda}(1+\mathrm{i}k\lambda)}]\\ &-\frac{\lambda\boldsymbol{Q}}{d(1-\mathrm{i}k\lambda)}[\mathrm{e}^{-\frac{d}{2\lambda}(1-\mathrm{i}k\lambda)}-\mathrm{e}^{\frac{d}{2\lambda}(1-\mathrm{i}k\lambda)}].\end{aligned}\tag{9}$$

According to Eqs. (8) and (9), $\boldsymbol{\tau}_k$ and $\boldsymbol{\tau}_{-k}$ takes considerable values while k has the same order with $\frac{2\pi}{d}$, indicating that the lowest order standing wave modes can be excited. For the symmetrical modes, $\boldsymbol{m}_k=\boldsymbol{m}_{-k}$ and $\boldsymbol{m}_{\mathrm{swk}}=\boldsymbol{m}_k(\mathrm{e}^{\mathrm{i}kx}+\mathrm{e}^{-\mathrm{i}kx})\propto\cos(kx)$, where $\boldsymbol{m}_{\mathrm{swk}}$ refers to the magnetization of the standing wave with wave vector k. The excitation efficiency is proportional to $\boldsymbol{\tau}_k+\boldsymbol{\tau}_{-k}$. In W(4 nm)/Py(9 nm)/Pt(2 nm) samples, $\boldsymbol{P}$ and $\boldsymbol{Q}$ have the same sign, and $\boldsymbol{\tau}_k+\boldsymbol{\tau}_{-k}$ which is a considerable value, indicating the excitation of symmetrical standing wave modes. According to the boundary condition, the integration of $\boldsymbol{m}$

in the thickness direction for symmetrical modes is nonzero, therefore, the standing wave signal can be detected. Additional details are provided in Section S4 of the SM.

To investigate THz intensity dependence of spin resonance signals, we attenuated THz radiation using wire-grid polarizers. The first polarizer was rotated to 0°, 20°, and 40° to modulate field amplitudes while the second maintained co-polarized alignment with the incident THz field. Figure 4(b) demonstrates the proportional relationship between Zeeman torque signal amplitude and THz field strength. The normalized signals can be seen in Section S5 of the SM. These results demonstrate that spin wave intensity is directly driven by strong-field THz radiation.

This study demonstrates robust strong-field THz magnetic field detection in Py through refined structural design and experimental validation. By employing Zeeman torque sampling, we extract THz waveforms without distortion even under strong-field conditions. This work characterizes the thickness-dependent response of ferromagnetic THz detectors across the range of 3–21 nm, showing enhanced sensitivity at a Py thickness of 21 nm within this range. Through structural optimization, we achieved effective strong-field THz detection in symmetric Ta(3 nm)/Py(9 nm)/Ta(3 nm) heterostructures. Compared with conventional EOS, this magnetic-field detection approach offers significant advantages such as elimination of polarization rotation saturation and reduced implementation costs. Furthermore, in asymmetric W(4 nm)/Py(9 nm)/Pt(2 nm) heterostructures featuring oppositely signed spin Hall angles, we observed not only THz magnetic component detection but also structure-induced spin waves originating from interfacial spin accumulation. This dual functionality establishes the proposed detector platform as a versatile tool enabling: distortion-free strong-field THz detection, intrinsic spin wave spectroscopy capabilities, and new pathways for developing next-generation spintronic memory devices.

Acknowledgements. This work was supported by the Scientific Research Innovation Capability Support Project for Young Faculty (Grant No. ZYGXQNJSKYCXNLZCXMI3), the National Key Research and Development Program of China (Grant No. 2022YFA1604402), the National Natural Science Foundation of China (Grant Nos. U23A6002, 92250307, and 52225106), and the Beijing Municipal Science and Technology Commission, Administrative Commission of Zhongguancun Science Park (Grant No. Z25110000692500).

References

[1] Koenig S, Lopez-Diaz D, Antes J, Boes F, Henneberger R, Leuther A, Tessmann A, Schmogrow R, Hillerkuss D, Palmer R, Zwick T, Koos C, Freude W, Ambacher O, Leuthold J, and Kallfass I 2013 *Nat. Photonics* **7** 977

[2] Nagatsuma T, Ducournau G, and Renaud C C 2016 *Nat. Photonics* **10** 371

[3] Ummethala S, Harter T, Koehnle K, Li Z, Muehlbrandt S, Kutuvantavida Y, Kemal J, Marin-Palomo P, Schaefer J, Tessmann A, Garlapati S K, Bacher A, Hahn L, Walther M, Zwick T, Randel S, Freude W, and Koos C 2019 *Nat. Photonics* **13** 519

[4] Yang Y, Yamagami Y, Yu X, Pitchappa P, Webber J, Zhang B, Fujita M, Nagatsuma T, and Singh R 2020 *Nat. Photonics* **14** 446

[5] Chaccour C, Soorki M N, Saad W, Bennis M, Popovski P, and Debbah M 2022 *IEEE Commun. Surv. Tutor.* **24** 967

[6] Hillger P, Grzyb J, Jain R, and Pfeiffer U R 2019 *IEEE Trans. THz Sci. Technol.* **9** 1

[7] Li X, Li J, Li Y, Ozcan A, and Jarrahi M 2023 *Light Sci. Appl.* **12** 233

[8] Federici J F, Schulkin B, Huang F, Gary D, Barat R, Oliveira F, and Zimdars D 2005 *Semicond. Sci. Technol.* **20** S266

[9] Malhotra I, Jha K R, and Singh G 2018 *Int. J. Microw. Wirel. Technol.* **10** 271

[10] Kawano Y 2012 *Laser Photonics Rev.* **6** 246

[11] Salén P, Basini M, Bonetti S, Hebling J, Krasilnikov M, Nikitin A Y, Shamuilov G, Tibai Z, Zhaunerchyk V, and Goryashko V 2019 *Phys. Rep.* **836–837** 1

[12] Salikhov R, Ilyakov I, Körber L, Kákay A, Gallardo R A, Ponomaryov A, Deinert J, de Oliveira T V A G, Lenz K, Fassbender J, Bonetti S, Hellwig O, Lindner J, and Kovalev S 2023 *Nat. Phys.* **19** 529

[13] Xiang Y, Jin Z, Hou L, Lan Z, Li Y, Peng Y, and Zhu Y 2025 *Chin. Phys. Lett* **42** 110403

[14] Hudl M, d'Aquino M, Pancaldi M, Yang S H, Samant M G, Parkin S S P, Dürr H A, Serpico C, Hoffmann M C, and Bonetti S 2019 *Phys. Rev. Lett.* **123** 197204

[15] Wang X, Zhang Y, Sun S, Li J, Cheng S, and Yang H 2025 *Chin. Phys. Lett.* **42** 047201

[16] Hu M, Zheng J, Cui K, Zhang W, and Huang Y 2024 *Electromagn. Sci.* **2** 1

[17] Li Z, Han H, Chao L, Chen Y, Chen G, and Huang W 2025 *Electromagn. Sci.* **3** 0090451

[18] Carr G L, Martin M C, McKinney W R, Jordan K, Neil G R, and Williams G P 2002 *Nature* **420** 153

[19] Wu X 2023 *Chin. Phys. Lett* **40** 054001

[20] Zhang B, Ma Z, Ma J, Wu X, Ouyang C, Kong D, Hong T, Wang X, Yang P, Chen L, Li Y, and Zhang J 2021 *Laser Photonics Rev.* **15** 2000295

[21] Wu X, Kong D, Hao S, Zeng Y, Yu X, Zhang B, Dai M, Liu S, Wang J, Ren Z, Chen S, Sang J, Wang K, Zhang D, Liu Z, Gui J, Yang X, Xu Y, Leng Y, Li Y, Song L, Tian Y, and Li R 2023 *Adv. Mater.* **35** 2208947

[22] Rouzegar R, Chekhov A L, Behovits Y, Serrano B R, Syskaki M A, Lambert C H, Engel D, Martens U, Münzenberg M, Wolf M, Jakob G, Kläui M, Seifert T S, and Kampfrath T 2023 *Phys. Rev. Appl.* **19** 034018

[23] Kim H, Kang C, Jang D, Roh Y, Lee S H, Lee J W, Sung J H, Lee S K, and Kim K Y 2024 *Light Sci. Appl.* **13** 118

[24] Hortensius J R, Afanasiev D, Matthiesen M, Leenders R, Citro R, Kimel A V, Mikhaylovskiy R V, Ivanov B A, and Caviglia A D 2021 *Nat. Phys.* **17** 1001

[25] Vaidya P, Morley S A, van Tol J, Liu Y, Cheng R, Brataas A, Lederman D, and del Barco E 2020 *Science* **368** 160

[26] Lan Z, Li Z, Xu H, Liu F, Jin Z, Peng Y, and Zhu Y 2024 *Chin. Phys. Lett.* **41** 044203

[27] Geng C, Su Y, Kong D, Yang Z, Li J, Cai J, Dai F, Song C, and Wu X 2024 *Opt. Lett.* **49** 4589

[28] Chekhov A L, Behovits Y, Martens U, Serrano B R, Wolf M, Seifert T S, Münzenberg M, and Kampfrath T 2023 *Phys. Rev. Appl.* **20** 034037

[29] Luo L, Mootz M, Kang J H, Huang C, Eom K, Lee J W, Vaswani C, Collantes Y G, Hellstrom E E, Perakis I E, Eom C B, and Wang J 2023 *Nat. Phys.* **19** 201

[30] Grishunin K, Mashkovich E A, Kimel A V, Balbashov A M, and Zvezdin A K 2021 *Phys. Rev. B* **104** 024419

[31] Mi X, Benito M, Putz S, Zajac D M, Taylor J M, Burkard G, and Petta J R 2018 *Nature* **555** 599

[32] Luo J, Lin T, Zhang J, Chen X, Blackert E R, Xu R, Yakobson B I, and Zhu H 2023 *Science* **382** 698
[33] Li F, Yu T, Lai J, Liu J, Liu P, Chen X, and Sun Y 2024 *Chin. Phys. Lett.* **41** 107301
[34] Gallot G and Grischkowsky D 1999 *J. Opt. Soc. Am. B* **16** 1204
[35] Leitenstorfer A, Hunsche S, Shah J, Nuss M C, and Knox W H 1999 *Appl. Phys. Lett.* **74** 1516
[36] Chekhov A L, Behovits Y, Heitz J J F, Syskaki M A, Jaiswal S, Gueckstock O, Serrano B R, Ruge A, Kredl J, Wolf M, Múnzenberg M, Jakob G, Kläui M, Seifert T S, and Kampfrath T 2025 *Sci. Adv.* **11** eadq7741